Acta Geochim (2026) 45:42–54
https://doi.org/10.1007/s11631-025-00821-7

ORIGINAL ARTICLE

Fe isotopes in sulfides in the Aguas Zarcas (CM2) chondrite: Implications for the history of the parent asteroids

Xinqian Zhu[1] · Xinyu Wang[1] · Cheng Qian[1] · Kexin Deng[1] · Qi He[1] · Zaicong Wang[1] · Wen Zhang[1] · Ao Yang[1] · Fabin Pan[1] · Xiang Wu[1]

Received: 3 April 2025 / Revised: 21 July 2025 / Accepted: 21 August 2025 / Published online: 23 September 2025

Abstract CM chondrites contain valuable insights into the formation and evolution of the solar nebula, as well as the secondary aqueous alteration processes that affected their parent bodies. Our study focuses on primary and secondary sulfides within the Aguas Zarcas (CM2) chondrite, investigating their formation mechanisms based on their morphology, textures, and compositions. Moreover, we infer the formation temperatures of the sulfides from 230 to 500 ℃ for primary and from 100 to 135 ℃ for secondary. We select representative grains and conduct Fe isotope measurements on them. The primary sulfides with $\delta^{56/54}$Fe ranging from − 2.44‰ to + 0.69‰ are associated with sulfide–silicate melt segregation, while secondary sulfides with $\delta^{56/54}$Fe values between − 1.83‰ and − 0.14‰ are linked to aqueous alteration. Overall, the Ni content of the grains is positively correlated with $\delta^{56/54}$Fe. It might be related to the changes in crystal structure and chemical bond lengths due to the increase in nickel content. Fe isotopes provide a new perspective on sulfide formation and the evolution of a carbonaceous chondrite parent body.

Keywords Aguas Zarcas · Fe isotopes · Chondrite · Sulfide

Supplementary Information The online version contains supplementary material available at https://doi.org/10.1007/s11631-025-00821-7.

✉ Xiang Wu
wuxiang@cug.edu.cn

[1] State Key Laboratory of Geological Processes and Mineral Resources, School of Earth Sciences, China University of Geosciences, Wuhan 430074, China

1 Introduction

Chondrites consist of three major components: chondrules, refractory inclusions, and matrix. The sulfides found in chondrites are the result of two generations, primary (nebular) and secondary (parent body alteration), consisting mainly of pyrrhotite ($Fe_{1-x}S$), pentlandite ($(Fe, Ni)_9S_8$), troilite (FeS), and pyrite (FeS_2). In CM chondrites, pyrrhotite dominates both generations and pentlandite as a subordinate phase in secondary assemblages. Pyrite abundance increases with the degree of aqueous alteration (Bullock et al. 2005; Schrader et al. 2021). Furthermore, prolonged aqueous alteration drives the oxidation of pyrrhotite and pyrite to magnetite (Fe_3O_4) (Singerling and Brearley 2020). These sulfides may occur in chondrules or as fragments in the matrix and offer insights into the fO_2 and fS_2 conditions during their formation and alteration (Schrader and Zega 2019; Schrader et al. 2021). The presence of troilite and metal aggregates indicates metamorphic equilibration at an fS_2 corresponding to the iron-troilite buffer (Harries and Langenhorst 2013). Sulfides are also highly sensitive to alteration processes on the parent body (Singerling and Brearley 2020), with the decrease in at.% Fe/S ratio of pyrrhotite reflecting an increase in the degree of aqueous alteration (i.e., Fe/S of pyrrhotite in CI < CM1 < CM2) (Bullock et al. 2005; Harries and Zolensky 2016; Schrader et al. 2021).

The primary sulfides are formed in the solar nebula through various processes, including sulfidization via the reaction of Fe–Ni metal with H_2S gas (Zanda et al. 1995; Lauretta et al. 1996) and crystallization via the condensation of monosulfide solid solution (mss) in chondrules during cooling after the chondrule formation event(s) (Harries and Langenhorst 2013; Schrader et al. 2016; Singerling and Brearley 2018). These high-temperature sulfides contain valuable information about the protoplanetary disk,

effectively constraining the origin and formation conditions of chondrites (Desch et al. 2012; Schrader et al. 2018; Holt and Herd 2022). By analyzing sulfide composition, Schrader et al. (2018) demonstrated that chondrule cooling rates were approximately 10^0 to 10^1 K/h between 873 and 503 K, inferring a background temperature of the protoplanetary disk <503 K. The secondary sulfides are products of interaction between fluid and metal or troilite, which formed during aqueous alteration of the parent body (Visser et al. 2019; Holt and Herd 2022). In the most aqueously altered CR meteorites, pyrrhotite can be oxidized to form magnetite (Singerling and Brearley 2020).

Iron (Fe), the most abundant metallic element in the Solar System, exhibits isotopic fractionation during planetary differentiation and asteroidal processes (Weyer et al. 2005; Sossi et al. 2016). While bulk Fe isotopic compositions of chondrites are strikingly homogeneous ($\delta^{56}/^{54}$Fe ≈ 0‰; Zhu et al. 2001; Wang et al. 2013), this uniformity likely masks critical fractionation signals between metal, sulfides, and silicates—a consequence of averaging effects in bulk analyses (Craddock and Dauphas 2011) and isotopic resetting by secondary alteration (Hezel et al. 2018). Recent advances in in situ microanalysis now enable spatially resolved isotopic measurements (Visser et al. 2019; Schiller et al. 2020; Nakanishi et al. 2022), offering a path to disentangle chondrule condensation signatures from parent body alteration imprints. Fe isotope fractionation in sulfide–silicate systems provides critical insights into planetary processes. Sulfides such as pyrrhotite exhibit lighter Fe isotopic compositions relative to coexisting silicate melts, as demonstrated by Schuessler et al. (2007), while kinetic effects during melt segregation may amplify this contrast (Ni et al. 2020). These fractionations make Fe isotopes a powerful tool for decoding formation environments and process drivers.

Aguas Zarcas, a CM2 chondrite, was quickly collected after falling on 23 April 2019 (Gattacceca et al. 2020), thus minimizing contamination from terrestrial weathering processes. Detailed studies by Kerraouch et al. (2021, 2022) have reported its petrological, mineralogical, chemical, isotopic (O, Ti, and Cr), and organic characteristics. Aguas Zarcas is a complex breccia that may have originated from several precursor parent bodies and undergone impact brecciation, mixing, and reassembly (Kerraouch et al. 2021, 2022). In addition, the discovery of compact fragments in Aguas Zarcas, along with the redistributed average abundance of Fe due to a strong shock event, indicates an active pebble transport event on its parent body, similar to what occurred on Bennu (Lauretta et al. 2019; Yang et al. 2022). Recent petrographic and compositional analyses of sulfides in Aguas Zarcas lithologies demonstrate that pyrrhotite Fe/S ratios reflect intense aqueous alteration (Schrader et al. 2021). These characteristics position Aguas Zarcas as a key sample to address unresolved questions in CM chondrite evolution, such as the thermal conditions of aqueous alteration, impact mixing-induced lithological variation, and the preservation of protoplanetary disk signatures in chondrites.

In this work, we focus on the sulfides in Aguas Zarcas, utilizing a combination of petrography, mineral chemistry, and in situ Fe isotope measurements to: (1) resolve chondrules condensation processes through isotope signatures of primary sulfides, correlating their $\delta^{56}/^{54}$Fe values to condensation temperatures and melt segregation processes; (2) examine the effects of aqueous alteration on Fe isotopes in secondary sulfides; and (3) decipher crystal-chemical controls on isotope fractionation by correlating Ni content and exsolution textures with isotope trends, building on bond-strength models for Fe–Ni–S systems (Liu et al. 2022; Polyakov and Soultanov 2011). This multi-scale approach bridges asteroidal processes with mineral-scale isotopic records, constraining how early high-temperature processes during chondrule formation and parent body environments collectively shaped CM chondrite evolution.

2 Methods

We divided the initial 4-g Aguas Zarcas sample into smaller pieces, selecting two of them to create thick sections with a 1-inch (c. 2.54-cm) diameter. These sections underwent a series of sanding processes, starting with rough sanding using 600- and 1200-grit sandpaper made of Si carbide, followed by fine sanding with 3000- and 5000-grit sandpaper. Subsequently, the sections were mechanically polished using 0.05-μm Al_2O_3 suspension, ultrasonically cleaned with ethanol, and then dried. In the sample we studied, we distinguished two lithologies, Met-2 and CM-clast, that exhibited textural and mineralogical similarities to those detailed in Kerraouch et al. (2021). All the experiments and measurements were conducted at the State Key Laboratory of Geological Processes and Mineral Resources (GPMR), China University of Geosciences, Wuhan, China.

The petrographic observations were performed on two scanning electron microscopes (Quanta 450 FEG and Helios G4) using backscattered electron (BSE) imaging and energy dispersive spectrometer (EDS) analysis. The mineral chemical compositions of the sulfides and metal were determined with JEOL JXA-8100 and JXA-8230 electron probe microanalyzers (EPMA). Both instruments were operated at 15 keV, with a beam current of 20 nA and a spot diameter of 1 μm. All the results have been reduced with the ZAF correction procedure. For the sulfides, natural and synthetic standards were used for wavelength dispersive spectrometry: Se (Se), pentlandite (S, Ni, Fe), cobalt metal (Co), chromite (Cr), and copper metal (Cu). For other minerals, the following natural and synthetic standards were used: sanidine (K), pyrope (Al, Fe), diopside (Ca), olivine (Si, Mg),

jadeite (Na), rhodonite (Mn), rutile (Ti), chromium oxide (Cr), pyrite (S), and nickel metal (Ni).

The Fe isotope compositions were measured using a Neptune Plus MC-ICP-MS (Thermo Fisher Scientific, Bremen, Germany) coupled with a 257-nm Yb fs-LA system (NER-FeomtoUC, USA) at GPMR. In the laser ablation system, helium was used as the carrier gas and mixed with argon (makeup gas) after the ablation cell. The single spot ablation mode was used, with the total acquisition time for each measurement approximately 63 s, including background signal, ablation signal acquisition, and washout. In addition, a new "wave" single-smoothing device was utilized to eliminate the short-term signal variation, especially for the slow pulse frequency condition (Hu et al. 2015). Detailed instrumental settings and operating conditions are summarized in Table 1.

Two in-house isotopic reference materials were used in this study, with HEM-1 as monitoring standards and L1-Po ($\delta^{56/54}$Fe = – 0.62 ± 0.07‰ relative to IRMM-014) were used as correction standards (Feng et al. 2024). The HEM-1 standard was obtained by sintering hematite powder pellets in an alumina crucible at 1000 ℃ for 2 h in a muffle furnace under an Ar atmosphere (Lü et al. 2024). The correction standard reference L1-Po is a natural pyrrhotite collected from the Linglong golden deposit located in the Jiaodong area of the North China Craton. Numerous LA-MC-ICP-MS measurements were analyzed by Feng et al. (2024). The results show that L1-Po has well-characterized and isotopically homogeneous properties. Repeated measurements of the monitoring standard were $\delta^{56/54}$Fe = 0.43 ± 0.04‰, which is consistent within the error range with the results of $\delta^{56/54}$Fe = 0.45 ± 0.04‰ measured by Lü et al. (2024). The sample-standard bracketing method was used with the following analytical sequence: L1-Po, sulfide, L1-Po. The detailed HEM-1 preparation process and correction method of measurements were described by Lü et al. (2024). The measured Fe isotope data were normalized relative to the conventional reference material IRMM-014 to compare with literature data. After renormalization, the ^{56}Fe/^{54}Fe ratio was converted into $\delta^{56/54}$Fe according to

$$\delta^{56/54}\mathrm{Fe}_{\mathrm{sample}} = \left(\frac{^{56}\mathrm{Fe}/^{54}\mathrm{Fe}_{\mathrm{sample}}}{^{56}\mathrm{Fe}/^{54}\mathrm{Fe}_{\mathrm{L1-Po}}} - 1\right) \times 1000[‰] - 0.62$$

Table 1 Operating parameters for Fe isotopic measurements by fs LA-MC-ICP-MS

Neptune plus MC-ICP-MS	
RF power	1200 W
Cool gas flow rate	16.3 L min^{-1} Ar
Auxiliary gas flow rate	1.3 L min^{-1} Ar
Sample gas flow rate	1.1 L min^{-1} Ar
Instrument resolution	High (7000)
Extraction	− 2000 V
Focus	− 729.8 V
Interface cones	X skimmer cone + jet sample cone
Collector configuration	L2 (^{52}Cr), L1 (^{53}Cr), C (^{54}Fe + ^{54}Cr), H1 (^{56}Fe), H2 (^{57}Fe)
Cycles/blocks	1 cycle/120 blocks
Integration time	0.524 s
Spray chamber	Quartz type with double-pass Scott design
Laser ablation system	
Laser type	Yb fs-LA system (NWR-FemtoUC, USA)
Wavelength	257 nm
Pulse width	300 fs
Fluence	2.88 J/cm^2
Ablation mode	Single spot
Spot size	30 μm
Repetition rate	10 Hz

3 Results

3.1 Petrography and mineral chemistry

Aguas Zarcas, a fallen meteorite, exhibits minimal terrestrial weathering ensuring the excellent preservation of its metal and sulfides. In this study, the samples have been categorized into three parts based on their lithology and degree of aqueous alteration: MET, MAX, and CM-like (Fig. 1). According to the classification of Kerraouch et al. (2021), the MET in this study corresponds to Met-2, while MAX and CM-like belong to the CM-clast.

MET is an unusual carbonaceous lithology and is characterized by a substantial presence of metal (Fig. 1a), and sulfides, phyllosilicates, and carbonates. Silicates are found in the chondrules and as isolated grains in the matrix. The modal abundance of metal and sulfides in MET is 3 vol%, with most of the opaque grains being metal. In addition to the high abundance of metal and sulfides, another characteristic of MET is that the coarse grains are not surrounded by a fine-grained rim.

Metal grains occur in both chondrules and matrix in MET. Within the chondrules, the metal typically exhibits spherical to ellipsoidal shapes, ranging from 1 to 100 μm in size, and comprising kamacite and Ni-rich metal (> 7.5 wt% Ni) (Fig. 1e). The metal grains found in certain chondrules exhibit a heterogeneous composition, featuring numerous Ni-rich grains (Fig. 1f). This intergrowth texture of internal metal is characterized as a fine-grained plessitic intergrowth of kamacite and tetrataenite. Such a morphology was also observed in ordinary chondrites and was interpreted as the result of thermal metamorphism on the parent body (Meftah

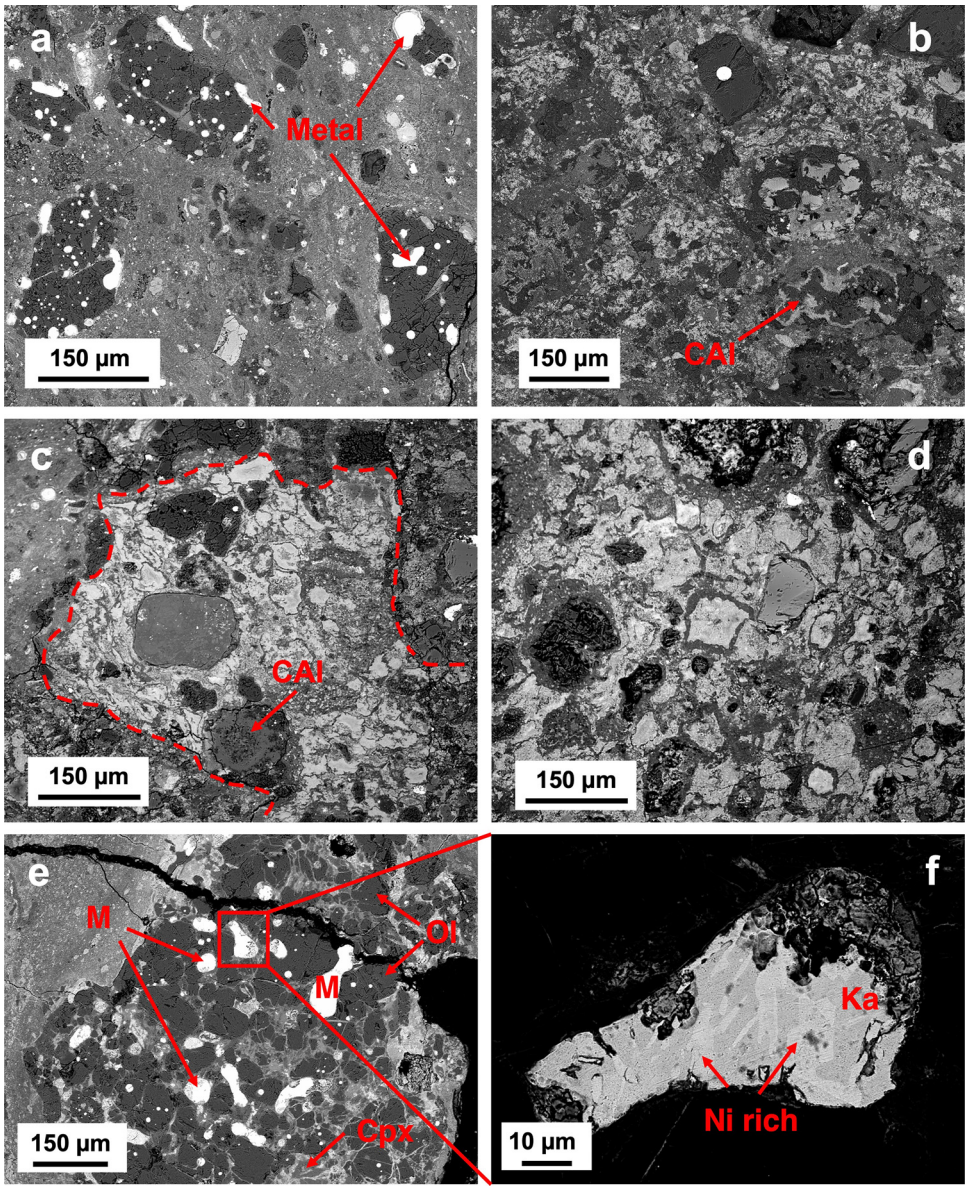

Fig. 1 BSE images for three petrographic categories of Aguas Zarcas. **a** MET, **b** MAX, **c** and **d** CM-like, **e** chondrule in MAX, **f** metal in chondrule

et al. 2016; Okabayashi et al. 2019; Gilmour et al. 2020; Florin et al. 2023). However, the Ni content of the Ni-rich metal in our study is not high enough to be taenite.

Most of the matrix belongs to MAX with typical lithology of CM2 chondrites (Fig. 1b), consisting of phyllosilicate, olivine, pyroxene, sulfides, and carbonates. Most of the chondrules display relatively regular round or ellipsoidal shapes, with diameters ranging widely from 120 to 890 μm. Additionally, calcium–aluminum-rich inclusions (CAIs) are observed in this sample, comprising spinel and hibonite surrounded by fine Fe-rich grains. The matrix is predominantly composed of phyllosilicates, tochilinite–cronstedtite intergrowths (TCI), and various mineral fragments like olivine, pyroxene, and sulfides. TCI is flocculent or acicular, replacing olivine in whole or in part, but retaining the hexagonal pseudomorph of olivine. We conducted EPMA measurements on the olivine, pyroxene, hibonite, and spinel. The detailed EPMA data of the composition are listed in Table S1. The sub-micron grain size of matrix phyllosilicates indicates a hydrated material and the composition of representative TCI is summarized in Table S2.

Metal grains in the matrix exist as clasts, displaying irregular shapes, although there are also spherical grains present. The metal within the matrix consists mainly of kamacite, with one exception of Ni-rich metal. The sizes of these grains range from 10 to 150 μm, with an average of 50 μm. In addition, certain grains are surrounded by a thin sulfide rim.

CM-like lithologies are close to MAX but there are some differences (Fig. 1c and d). Isolated large-diameter silicates

(50–150 µm) are more abundant in the CM-like matrix than in the MAX matrix, and the CAIs retain the rounded shape. In addition, the CM-like shows a lower degree of aqueous alteration, which will be discussed in Sect. 4.1.

3.2 Texture and composition of Fe-Ni sulfides

In both sections, numerous metal and sulfides are present within the chondrules and matrix. These grains are classified into three groups based on their texture and composition: (1) pyrrhotite–pentlandite intergrowth (PPI) with an exsolution texture; and (2) sulfide without exsolution texture.

3.2.1 Pyrrhotite–pentlandite intergrowth (PPI)

The PPI grains occur in chondrules and matrix, range in size from 10 to 150 µm, and are primarily composed of pyrrhotite (Po) and pentlandite (Pn), displaying various exsolution textures such as patches, blades, lamellae, and snowflake (Fig. 2). Individual grains can exhibit two or even three different exsolution textures simultaneously. In most cases, pentlandite is typically observed in the form of rod or patch exsolutions within pyrrhotite, but there are also instances of pyrrhotite exsolutions in the pentlandite.

Irregularly shaped pentlandite patches were often observed surrounding the grains (Fig. 2a and b). Pentlandite blades share a resemblance to rods but are larger and thicker (Fig. 2c). Pentlandite lamellae, on the other hand, are long, narrow strips characterized by an oriented arrangement, frequently coexisting with rods and blades (Fig. 2c). Some pentlandite patches or grains display snowflake texture (Fig. 2d), a phenomenon previously reported by Schrader et al. (2015). Submicron pyrrhotite blades and patches aggregate to create a dendrite-like structure, clustering to form the distinctive snowflake exsolution texture. Table 2 presents representative electron microprobe analyses of PPI.

3.2.2 Unexsolved sulfide

Some sulfides are homogeneous in composition and lack exsolution textures. These grains exhibit irregular shapes and are found within the matrix as clasts. These grains vary in size from a few to 80 µm, with an average size of 30 µm (Fig. 3a and b). Approximately half of these grains consist of pyrrhotite, while the remainder contain pentlandite.

Unexsolved sulfide grains, some as small as 1 µm or even sub-micron in diameter, are clustered at the peripheries of the chondrules (Fig. 3c). The EMPA data reveal that these grains can consist of either pyrrhotite or pentlandite, yet their minuscule size hinders precise composition analysis. Additionally, we observed some rounded magnetite

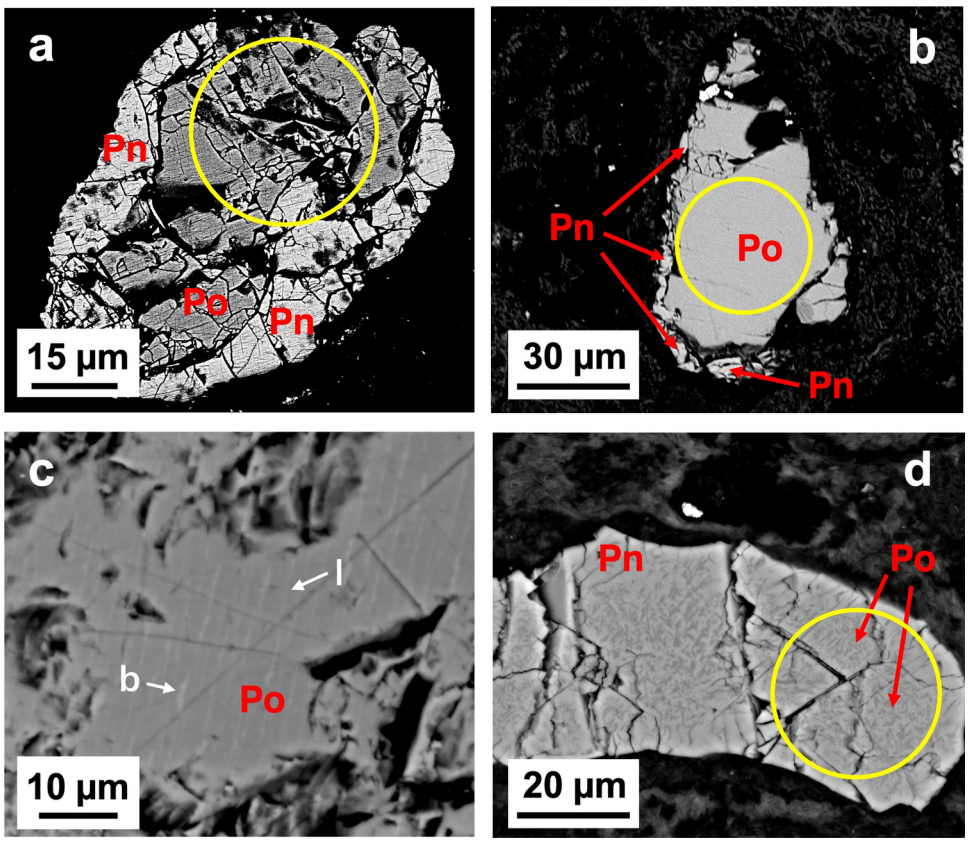

Fig. 2 BSE images of PPI grains. **a** and **b** PPI with Pn patches. **c** PPI with Pn blades and lamellae. **d** PPI with snowflake texture. *Yellow circles* represent LA-MC-ICP-MS points. *b* blade, *l* lamellae *Pn* pentlandite, *Po* pyrrhotite, *s* snowflake

Table 2 Major and minor element compositional averages and ranges of sulfides and metal (wt%)

Type	Phase	Number of analyses		Se (wt%)	S (wt%)	Ni (wt%)	Co (wt%)	Cr (wt%)	Fe (wt%)	Cu (wt%)	Total (wt%)
PPI	Pyrrhotite	12	Range	bdl-0.06	34.72–38.81	0.66–15.98	0.17–0.80	0.01–0.09	47.90–60.90	bdl-0.07	
			Average	0.02 ± 0.02	37.44 ± 1.46	4.60 ± 5.42	0.41 ± 0.21	0.04 ± 0.02	57.15 ± 4.33	0.03 ± 0.02	99.78 ± 0.56
	Pentlandite	12	Range	bdl-0.04	32.18–34.22	20.16–32.50	0.57–1.11	bdl-0.05	33.75–45.45	bdl-0.15	
			Average	0.01 ± 0.01	33.41 ± 0.54	30.03 ± 3.22	0.81 ± 0.15	0.02 ± 0.02	35.88 ± 3.02	0.04 ± 0. 04	100.24 ± 0.54
Sulfide	Pyrrhotite	13	Range	bdl-0.08	37.32–39.42	0.24–4.21	0.12–0.64	bdl-0.34	56.83–61.23	bdl-0.22	
			Average	0.02 ± 0.03	38.13 ± 0.65	1.93 ± 2.26	0.33 ± 0.19	0.06 ± 0.08	58.94 ± 2.08	0.03 ± 0.06	99.56 ± 1.33
	Pentlandite	11	Range	bdl-0.08	32.53–33.74	28.15–34.21	0.67–2.62	0.01–0.04	28.91–35.61	0.02–0.09	
			Average	0.02 ± 0.02	33.18 ± 0.38	32.29 ± 1.93	1.54 ± 0.64	0.03 ± 0.01	32.23 ± 2.12	0.05 ± 0.02	99.34 ± 2.66
Metal	Kamacite	45	Range	bdl-0.05	0.01–0.14	4.35–6.68	0.34–0.56	bdl-0.93	91.89–95.30	bdl-0.17	
			Average	0.01 ± 0.01	0.04 ± 0.03	5.32 ± 0.50	0.42 ± 0.05	0.40 ± 0.26	93.31 ± 0.78	0.06 ± 0.05	99.80 ± 0.57
	Ni-rich metal	5	Range	bdl-0.05	0.01–0.04	9.39–19.97	0.40–1.00	0.04–0.69	79.39–89.73	bdl-0.04	
			Average	0.01 ± 0.02	0.02 ± 0.01	13.22 ± 3.55	0.53 ± 0.24	0.54 ± 0.25	85.92 ± 3.48	0.02 ± 0.02	100.37 ± 0.51

Range minimum–maximum; *Average* ± one standard deviation

bdl below detection limit

aggregates in the matrix, which implies that some of the sulfides were oxidized during aqueous alteration (Fig. 3d).

The compositions of unexsolved pyrrhotite and pentlandite are detailed in Tables 2 and S3. The more Ni-rich pyrrhotite (10.15 wt%) data points are likely to be analyses of pyrrhotite which contains submicron rods of exsolved pentlandite that overlap with the electron beam.

3.3 Fe isotopic composition of sulfides

We have studied 17 sulfide grains from Aguas Zarcas (Tables 3 and S3, and Fig. S2). Sulfides include PPI with various exsolved texture, unexsolved pyrrhotite, and unexsolved pentlandite. All of them have large enough surfaces to ensure that there is no interference from surrounding materials within the laser ablation range. All measured samples aligned along a single mass-dependent fractionation line with a slope of 1.36, and a *y*-axis intercept of − 0.01 (Fig. S1). The measured Fe isotope data are normalized relative to IRMM-014. The $\delta^{56/54}$Fe values of sulfides range from − 2.44‰ to 0.69‰ (Fig. 4). Notably, there are significant discrepancies in the $\delta^{56/54}$Fe compositions between PPI grains in Aguas Zarcas. In contrast, unexsolved sulfides display a distinct Fe isotope composition from the bulk, with most sulfides showing negative $\delta^{56/54}$Fe values.

4 Discussion

4.1 Degree of alteration

CM chondrites contain abundant phyllosilicates such as cronstedtite and other serpentine phases, alongside tochilinite carbonates, secondary sulfides, and oxides, resulting from a relatively homogeneous aqueous alteration in the parent asteroid (Zolensky et al. 1997; Lee and Ellen 2008; Velbel and Palmer 2011; Howard et al. 2015). Various degrees of aqueous alteration have resulted in changing mineral composition and texture (Browning et al. 1996). During the aqueous alteration process, CM chondrites may exhibit features such as serpentine–tochilinite intergrowth generation, matrix hydration, chondrule phenocryst alteration, Fe–Ni metal oxidation, and changes in carbonate mineralogy. Rubin et al. (2007) concluded a new petrologic subtype classification system based on mineralogical and textural features to reflect the extent of progressive alteration, ranging from subtype 2.0 (highly altered) to 2.6 (moderately altered). In Rubin's classification, with increasing degree of aqueous alteration, there is a significant increase in both S/SiO_2 and FeO/SiO_2 in TCI. Lentfort et al. (2021) further refined this classification by suggesting that accurate subtype classification could be achieved by solely considering the FeO/SiO_2

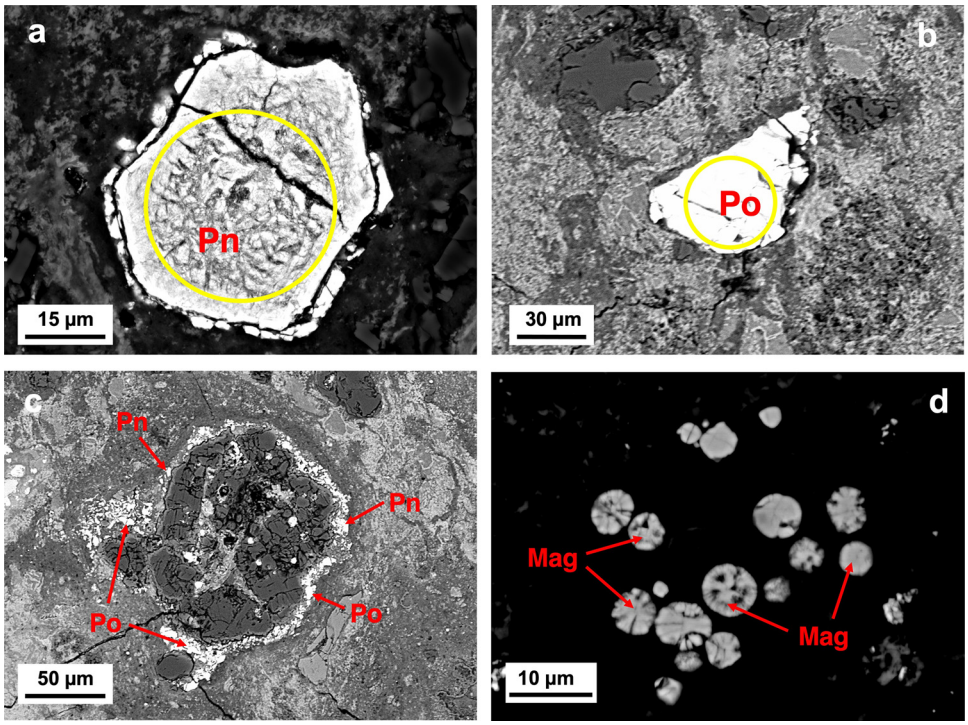

Fig. 3 BSE images of unexsolved sulfides and magnetite: **a** unexsolved Pn, **b** unexsolved Po, **c** sulfide rim at the edge of the chondrules, **d** magnetite occurring in the matrix. *Yellow circles* represent LA-MC-ICP-MS points. *Cpx* Ca-rich pyroxene, *Ka* kamacite, *M* metal, *Mag* magnetite, *Ol* olivine, *Pn* pentlandite, *Po* pyrrhotite

Table 3 Chemical composition and Fe isotope composition of sulfides and metal

Sample	S (wt%)	Fe (wt%)	Ni (wt%)	δ^{56}Fe (‰)	2SD
PPI-1	36.23	54.84	8.13	− 2.44	0.12
PPI-2	36.10	46.41	16.87	− 1.14	0.11
PPI-3	36.02	47.46	15.395	− 0.67	0.12
PPI-4	35.72	46.84	16.865	− 0.77	0.14
PPI-5	34.20	42.84	21.82	0.69	0.12
PPI-6	33.55	34.35	31.96	0.21	0.13
PPI-7	35.70	47.66	15.945	− 1.11	0.12
PPI-8	36.23	52.92	10.82	− 0.49	0.11
PPI-9	35.17	47.86	15.945	− 0.97	0.11
PPI-10	37.83	59.14	2.71	− 1.33	0.12
Po-1	37.95	57.82	2.89	− 1.83	0.13
Po-2	38.06	58.67	2.00	− 1.43	0.12
Po-3	38.11	59.36	0.36	− 1.48	0.15
Po-4	38.43	60.56	0.65	− 1.44	0.11
Po-5	37.01	53.20	8.68	− 1.14	0.14
Pn-1	32.53	28.91	31.23	− 0.14	0.13
Pn-2	33.20	31.40	34.21	− 0.57	0.14

Pn pentlandite, *Po* pyrrhotite, *PPI* pyrrhotite–pentlandite intergrowth

ratio in the composition of TCI, expanding Rubin's scale to encompass subtypes 2.0–2.9.

The Aguas Zarcas is a typical breccia including at least five different lithologies (Kerraouch et al. 2021). Clasts of different lithologies exhibit different degrees of aqueous alteration. We select 8 TCI in different characterized clasts for EPMA measurements and calculated their FeO/SiO_2 ratio. Various degrees of alteration have been identified by comparing them with the data already determined by Lentfort et al. (2021). Our samples are categorized into subtypes 2.0–2.2 for the majority of MAX and MET, and 2.7–2.8 for CM-like (Fig. 5), which is consistent with the results from Kerraouch et al. (2021). Aguas Zarcas exhibited varying degrees of aqueous alteration compared with other chondrites, which is likely related to the processes experienced by the parent body. Various degrees of aqueous alteration have occurred at different locations in the parent body, resulting in a change in lithology at each location. In later stages, due to certain events, the different lithologies were redistributed and experienced mixing and re-accretion to form a new complex breccia.

4.2 Fe isotope variations from different origins

4.2.1 Fe isotope variations in primary sulfides

PPI grains display the largest variation range among the Fe isotope compositions of all the grains, which is significantly related to the formation of the PPI. In the past, sulfides were generally considered to be the products of aqueous alteration processes. However, recent studies by Harries and Langenhorst (2013), Schrader et al. (2015), and Holt and Herd (2022) propose that primary sulfides, specifically PPI, may be preserved in carbonaceous chondrites. PPI are formed

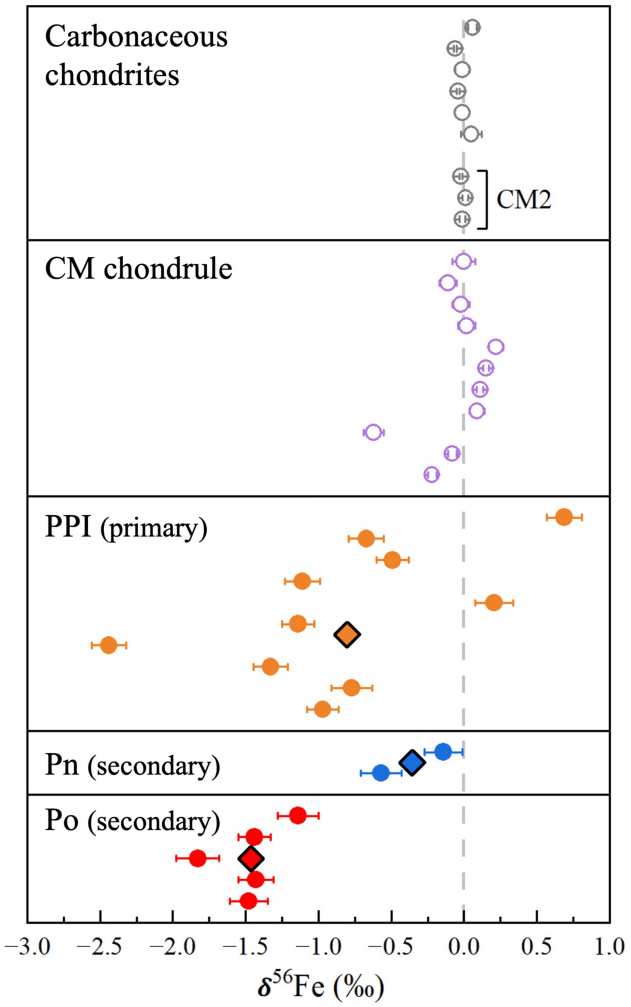

Fig. 4 Fe isotope composition of sulfides. The *solid symbols* are the data points from this study, the *open symbols* are the reference, and the *diamond symbols* are averages. Data of bulk carbonaceous chondrites are from Schiller et al. (2020), and data of CM chondrules are from Hezel et al. (2018)

by crystallization from an mss $(Fe, Ni)_{1-x}S$ melt. As the chondrule cooled, the Fe–Ni–S melt and silicate melt likely segregated. A subsequent temperature decrease led to the decomposition of mss into pyrrhotite and pentlandite at approximately 870 K (Kitakaze et al. 2011). The resultant grains typically tended to be PPI with various exsolution textures (Singerling and Brearley 2018; Holt and Herd 2022).

It has been extensively demonstrated that these complex exsolution textures are exclusively formed through crystallization, and different exsolution textures of sulfides emerge at varying temperatures (Durazzo and Taylor 1982; Kelly and Vaughan 1983; Etschmann et al. 2004). Therefore, the formation temperature of PPI can be limited by using the characteristics of the exsolution structure and composition (Fig. 6a). In Aguas Zarcas, nonlinear textures like blocks and patches were produced between 610 and 250 °C (Fig. 3a and b), while linear textures such as blades, rods, and lamellae formed between 250 and 150 °C (Fig. 3c), and flame textures arose below 150 °C. Initially, these exsolution textures consisted of minute pentlandite exsolutions, such as bods, which gradually enlarged over time given sufficient temperature conditions. Such a temperature range corresponds exactly to the temperature at which condensation and decomposition of mss melt occur. Therefore, it is reasonable to consider these PPI as primary products of high temperatures. These diverse PPI grains and exsolution textures have been observed and reported in various carbonaceous chondrites, including CM (Harries and Langenhorst 2013; Singerling and Brearley 2018), CR (Schrader et al. 2015; Singerling and Brearley 2018), CK (Schrader et al. 2016), CI (Berger et al. 2016), and C2-ung (Holt and Herd 2022).

We consider that the $\delta^{56/54}$Fe of PPI is probably related to sulfide–silicate melt segregation, and the light $\delta^{56}/^{54}$Fe values of PPI relative to theoretical silicate compositions align with predicted equilibrium fractionation during mss–silicate melt segregation. Previous research has revealed that Fe isotopic fractionation between metal and silicate is minimal (Weyer et al. 2005; Hin et al. 2012; Liu et al. 2017). However, segregation between mss and silicate melts can lead to Fe isotope fractionation. Recent experimental studies by Ni et al. (2020) demonstrated that, during core crystallization of planetesimals, solid metal phases preferentially incorporate heavier Fe isotopes, while residual S-rich melts retain lighter isotopes. This mechanism aligns with our observations of lighter $\delta^{56/54}$Fe values in PPI sulfides compared to coexisting metal grains. The fractionation between sulfides and silicates is further supported by crystallization experiments and diffusion kinetics (Schuessler et al. 2007). This preference arises from distinct bonding environments: Fe^{2+} in sulfides favors light isotopes, whereas Fe^{2+} and Fe^{3+} in silicates accumulates heavier isotopes.

Kinetic isotope effects during Fe diffusion from metal to sulfide further enhance light isotope enrichment, as lighter Fe isotopes diffuse more rapidly under magmatic conditions (Ni et al. 2020). These effects are amplified during sulfide segregation, where non-equilibrium diffusion of light Fe isotopes into sulfides resembles the sub-solidus diffusion processes observed in iron meteorites (Chernonozhkin et al. 2016). Rapid crystallization or incomplete equilibration during melt migration likely preserves these isotopic signatures, reinforcing the contrast between sulfides and coexisting phases.

Although we have not conducted Fe isotope measurements on silicate, comparisons to IIIAB iron meteorites suggest that silicates should exhibit heavier $\delta^{56/54}$Fe than sulfides, consistent with fractional crystallization trends (Chernonozhkin et al. 2016). Thus, it is a reasonable speculation that the $\delta^{56/54}$Fe of silicate should be positive. The observed fractionation thus reflects a combination of

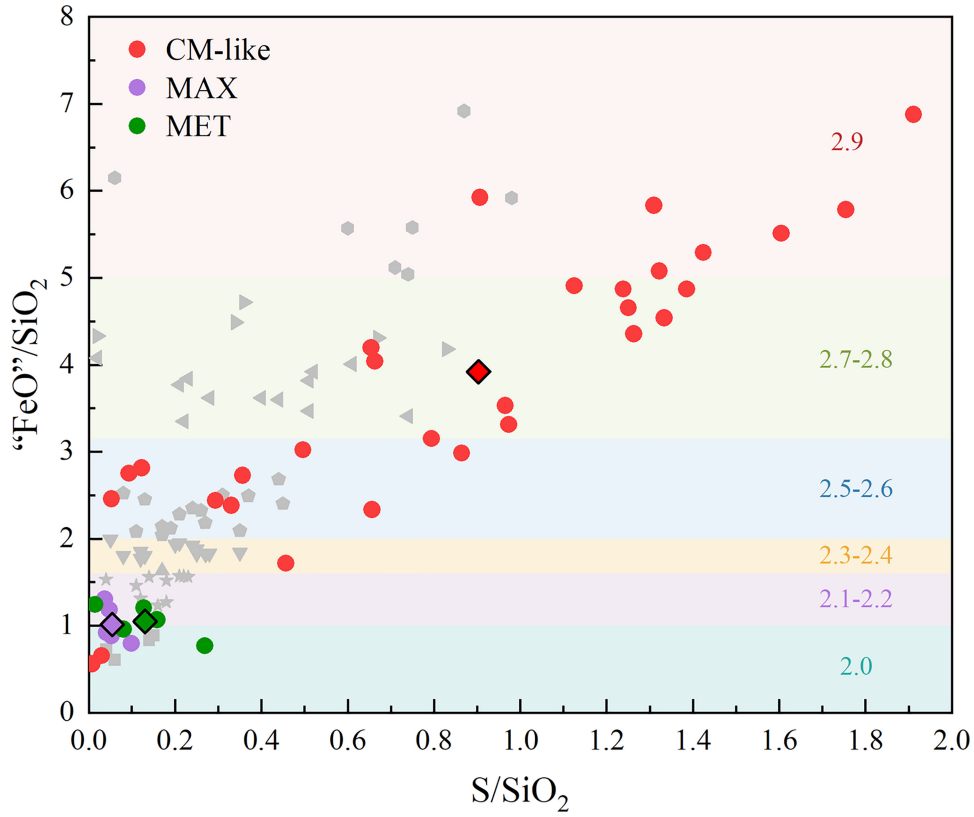

Fig. 5 FeO/SiO_2 versus S/SiO_2 for TCI in different lithologies in Aguas Zarcas. *Colored symbols* are data from this study, *gray points* are data from Lentfort et al. (2021), and the *diamond symbols* are mean values of corresponding color data

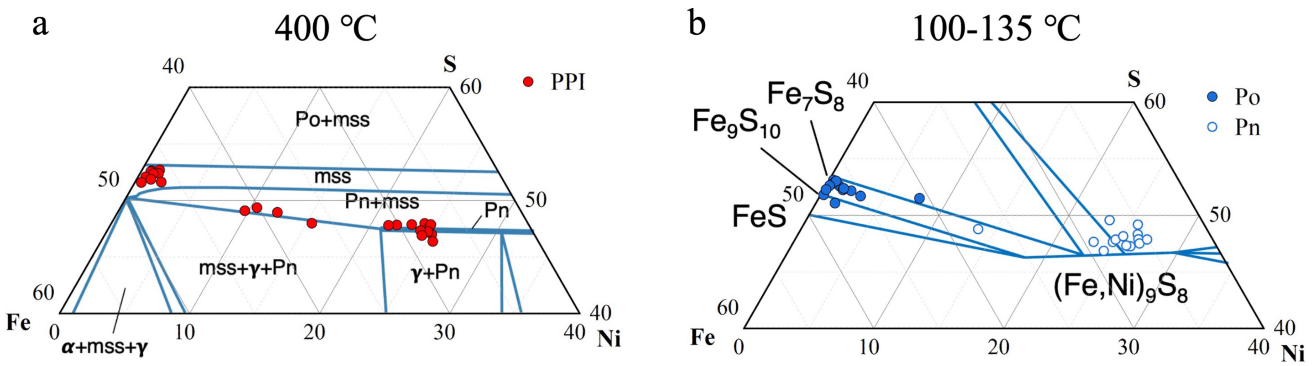

Fig. 6 Fe–Ni–S ternary phase diagrams with sulfide data from all the samples studied here. **a** 400 ℃; **b** 100–135 ℃. *Data points* represent a relatively separate analysis of one mineral phase. *mss* monosulfide solid solution, *Pn* pentlandite, *Po* pyrrhotite. Phase diagrams adapted from Raghavan (2004); original data from Naldrett (1989) (100-135 °C), Craig et al. (1968) (400 °C)

equilibrium bonding effects and kinetic diffusion. Furthermore, chondrule melting events can cause evaporation of volatile elements such as iron, potentially leading to isotopic fractionation. Supporting evidence for evaporation processes during chondrule formation is provided by the enrichment of heavy chromium isotopes observed within enstatite chondrite chondrules (Zhu et al. 2021).

4.2.2 Fe isotope variations in secondary sulfides

Unlike PPI, many unexsolved sulfides are not characterized as high-temperature products and are more like the result of secondary aqueous alteration on the parent body (Brearley et al. 2006). Petrological subtyping identifies that Aguas Zarcas experienced wide-ranging aqueous alteration.

The alteration process created a high oxygen fugacity environment, which could facilitate the formation of pentlandite under such conditions. The equilibrium temperatures of unexsolved sulfides in Aguas Zarcas are in the range of 100–135 °C (Fig. 6b), consistent with the temperature reached by aqueous alteration of CM chondrites (Alexander et al. 2014; Guo and Eiler 2007). Therefore, we attribute the unexsolved sulfide formation to secondary aqueous alteration.

These pyrrhotites generally contain lighter Fe isotopes compared to PPI and are likely related to aqueous alteration. Previous experimental investigations have revealed that equilibrium Fe isotope fractionation factors between fluids and minerals such as hematite, troilite, and magnetite can vary between 0‰ and 0.5‰, showing significant sensitivity to environmental conditions (Guilbaud et al. 2011; Saunier et al. 2011; Frierdich et al. 2014; Scott et al. 2017). For example, in the interaction between seafloor basalts and hydrothermal fluids, the Fe isotopes within sulfides progressively become lighter with decreasing temperature (Zeng et al. 2021). During low-temperature aqueous alteration, lighter Fe isotopes tend to partition into the fluid during interactions with silicates or metal. Consequently, sulfides formed at lower temperatures inherit lighter $\delta^{56/54}$Fe values from the surrounding fluid. Although Fe isotopic measurements were not conducted on the phyllosilicates in the matrix, it is plausible to speculate that these products of aqueous alteration may also contain lighter Fe isotopes.

4.2.3 Influence of Ni content on iron b-factors

A correlation between the Ni content and Fe isotopes in minerals was observed in our study (Fig. 7). We have shown that the $\delta^{56/54}$Fe of pentlandite is significantly heavier than pyrrhotite, even though they are both secondary sulfides. Meanwhile, we encountered two PPI grains displaying a snowflake exsolution texture that showed positive $\delta^{56/54}$Fe values. The snowflake exsolution texture means that the grains contain a higher Ni content than other PPI. This interesting observation also suggests the existence of a relationship between Ni content and Fe isotopes.

The atomic radius of nickel is 1.24 Å, slightly shorter than iron. Therefore, the incorporation of nickel induces lattice distortion in the sulfide, resulting in a shortening of the metal–sulfur bond length (Feng et al. 2014). A study of the equilibrium fractionation factors of Fe isotopes in b-(Ni, Fe) S solid solutions by using a first-principles method found that the Fe b-factor increases approximately linearly with increasing Ni content (Liu et al. 2022). As the Ni content increases, the sulfide gradually transforms into a Ni-controlled crystal structure instead of Fe (Feng et al. 2014), and the average metal–sulfur bond length also decreases. Shorter bonds with higher vibrational frequency and a greater bond

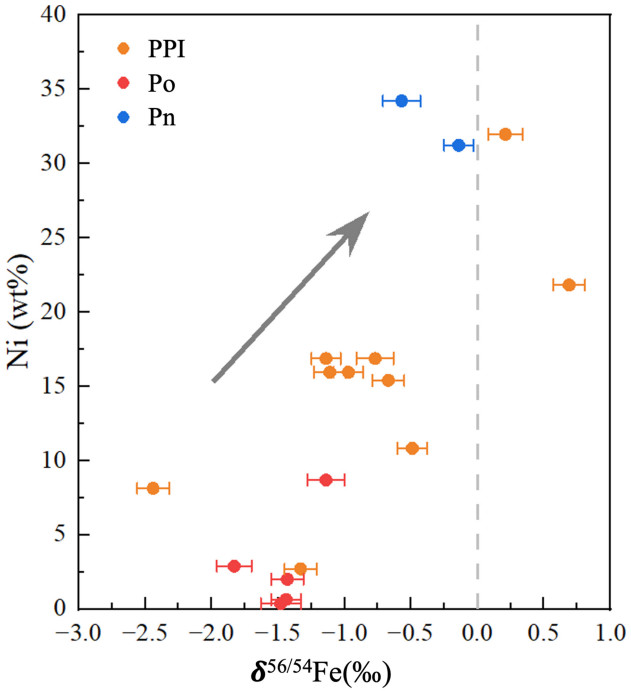

Fig. 7 $\delta^{56/54}$Fe vs. Ni content of sulfides. The grains' Fe isotope variations increase with increasing Ni content

stiffness make it easier to enrich in heavy isotopes (Bigeleisen and Mayer 1947; Schauble 2004; Feng et al. 2014), which explains why the $\delta^{56/54}$Fe values become heavier with increasing Ni content.

The b-factors of Fe-bearing minerals were investigated by Mossbauer spectroscopy and nuclear resonant inelastic X-ray scattering, successfully obtaining the Fe b-factor of magnetite, pyrite, hematite, chalcopyrite, and metallic iron (Polyakov 2009; Polyakov et al. 2019). Ferric compounds were identified with higher b-factors than ferrous compounds (Polyakov et al. 2007). In addition, the hybridization between the 3d orbitals of Ni and the 3p orbitals of S was stronger than that of Fe, leading to an enhanced covalency of the Fe–S bond (Polyakov and Soultanov 2011). Therefore, the incorporation of Ni may change the local electronic structure, thereby indirectly affecting Fe isotope fractionation.

5 Conclusions

This study has unraveled the formation history of sulfides in the Aguas Zarcas (CM2) chondrite through an integrated analysis of petrography, mineral chemistry, and in situ Fe isotope measurements.

Primary sulfides (PPI) were formed through nebular condensation as simultaneous products of chondrules. Monosulfide solid solution (mss) segregated from silicate melts

at ~ 950 °C and subsequently crystallized into pyrrhotite–pentlandite intergrowths during cooling (150-610 °C). The light $\delta^{56/54}$Fe values of PPI (− 2.44‰ to + 0.69‰) reflect preferential incorporation of light isotopes into sulfides during mss–silicate melt segregation, consistent with equilibrium fractionation dominated by Fe^{2+}-S bonding in pyrrhotite. Intragrain isotopic heterogeneity (e.g., pentlandite vs. pyrrhotite) likely arises from Ni-modulated variations in metal–sulfur bond lengths, which alter vibrational frequencies and isotope partitioning.

Secondary sulfides (unexsolved sulfide) formed during low-temperature aqueous alteration (100–135 °C) exhibit lighter $\delta^{56/54}$Fe values (− 1.83‰ to − 0.14‰). Aqueous alteration probably contributed to the secondary sulfides with light $\delta^{56/54}$Fe, while the range of $\delta^{56/54}$Fe variations was influenced by the Ni content.

Acknowledgements This research was supported by the National Science Foundation of China ((Nos.42225202 and 41827802). We are grateful to Shaofan Che for providing valuable suggestions for revising the article.

Authors' contributions XZ conceptualization, experimental design, performing experiments, data analysis, writing—original draft, writing—review and editing; XW performing experiments, data analysis, writing—original draft, writing—review and editing; CQ and KD performing experiments, data analysis, writing—review and editing; QH and ZW writing—review and editing, finalization assistance; WZ, AY and FP experimental technical support; XW sample provision, conceptualization, experimental design, writing—review and editing, finalization assistance.

Data availability Data are available through Mendeley Data at https://data.mendeley.com/datasets/8kbfb8jt45/5

Declarations

Conflict of interest The authors declare that they have no known competing financial interests or personal relationships that could have appeared to influence the work reported in this paper.

Appendix

Supplementary data associated with this article can be found in the online version, which includes the details of i) Selected areas of all isotope measurements; ii) representative mineral and TCI composition data in Aguas Zarcas; iii) Compositional data for sulfides and metal and corresponding Fe isotope data.

References

Alexander CMO, Cody GD, Kebukawa Y, Bowden R, Fogel ML, Kilcoyne ALD, Nittler LR, Herd CDK (2014) Elemental, isotopic, and structural changes in Tagish Lake insoluble organic matter produced by parent body processes. Meteorit Planet Sci 49(4):503–525. https://doi.org/10.1111/maps.12282

Berger EL, Lauretta DS, Zega TJ, Keller LP (2016) Heterogeneous histories of Ni-bearing pyrrhotite and pentlandite grains in the CI chondrites Orgueil and Alais. Meteorit Planet Sci 51(10):1813–1829. https://doi.org/10.1111/maps.12721

Bigeleisen J, Mayer MG (1947) Calculation of equilibrium constants for isotopic exchange reactions. J Chem Phys 15(5):261–267. https://doi.org/10.1063/1.1746492

Brearley AJ, Binzel RP, Walker RM (2006) The action of water. In: Lauretta DS, McSween HY, Binzel RP (eds) Meteorites and the early solar system II. University of Arizona Press, pp 587–624

Browning LB, McSween HY, Zolensky ME (1996) Correlated alteration effects in CM carbonaceous chondrites. Geochim Cosmochim Acta 60(14):2621–2633. https://doi.org/10.1016/0016-7037(96)00121-4

Bullock ES, Gounelle M, Lauretta DS, Grady MM, Russell SS (2005) Mineralogy and texture of Fe-Ni sulfides in CI1 chondrites: clues to the extent of aqueous alteration on the CI1 parent body. Geochim Cosmochim Acta 69(10):2687–2700. https://doi.org/10.1016/j.gca.2005.01.003

Chernonozhkin SM, Goderis S, Costas-Rodríguez M, Claeys P, Vanhaecke F (2016) Effect of parent body evolution on equilibrium and kinetic isotope fractionation: a combined Ni and Fe isotope study of iron and stony-iron meteorites. Geochim Cosmochim Acta 186:168–188. https://doi.org/10.1016/j.gca.2016.04.050

Craddock PR, Dauphas N (2011) Iron isotopic compositions of geological reference materials and chondrites. Geostand Geoanal Res 35(1):101–123. https://doi.org/10.1111/j.1751-908X.2010.00085.x

Craig J, Naldrett A, Kullerud G (1968) The Fe-Ni-S system: 400°C isothermal diagram. Carnegie Inst. Wash Yearbook 66:440–441

Desch SJ, Morris MA, Connolly HC Jr, Boss AP (2012) The importance of experiments: Constraints on chondrule formation models. Meteorit Planet Sci 47(7):1139–1156. https://doi.org/10.1111/j.1945-5100.2012.01357.x

Durazzo A, Taylor LA (1982) Exsolution in the mss-pentlandite system: Textural and genetic implications for Ni-sulfide ores. Miner Deposita 17(3):313–332. https://doi.org/10.1007/BF00204463

Etschmann B, Pring A, Putnis A, Grguric BA, Studer A (2004) A kinetic study of the exsolution of pentlandite $(Ni, Fe)_9S_8$ from the monosulfide solid solution (Fe, Ni)S. Am Mineral 89(1):39–50. https://doi.org/10.2138/am-2004-0106

Feng CQ, Qin T, Huang SC, Wu ZQ, Huang F (2014) First-principles investigations of equilibrium calcium isotope fractionation between clinopyroxene and Ca-doped orthopyroxene. Geochim Cosmochim Acta 143:132–142. https://doi.org/10.1016/j.gca.2014.06.002

Feng YT, Zhang W, Hu ZC, Luo T, Li QL, Liu JY (2024) New potential sulfide reference materials for microbeam S-Fe-Cu isotope measurements. Geostand Geoanal Res 48(1):227–244. https://doi.org/10.1111/ggr.12530

Florin G, Alard O, Luais B, Rushmer T (2023) Abundances of siderophile elements in H-chondrite metal grains: implications for the origin of metal in unequilibrated ordinary chondrites. Geochim Cosmochim Acta 341:1–15. https://doi.org/10.1016/j.gca.2022.11.014

Frierdich AJ, Beard BL, Scherer MM, Johnson CM (2014) Determination of the $Fe(II)_{aq}$–magnetite equilibrium iron isotope fractionation factor using the three-isotope method and a multi-direction approach to equilibrium. Earth Planet Sci Lett 391:77–86. https://doi.org/10.1016/j.epsl.2014.01.032

Gattacceca J, McCubbin FM, Bouvier A, Grossman JN (2020) The meteoritical bulletin, no. 108. Meteorit Planet Sci 55(5):1146–1150. https://doi.org/10.1111/maps.13493

Gilmour CM, Herd CDK (2020) *In situ* analysis of platinum group elements in equilibrated ordinary chondrite kamacite and taenite. Meteorit Planet Sci 55(3):679–702. https://doi.org/10.1111/maps.13436

Guilbaud R, Butler IB, Ellam RM, Rickard D, Oldroyd A (2011) Experimental determination of the equilibrium Fe isotope fractionation between Feaq2+ and FeSm (mackinawite) at 25 and 2 °C. Geochim Cosmochim Acta 75(10):2721–2734. https://doi.org/10.1016/j.gca.2011.02.023

Guo WF, Eiler JM (2007) Temperatures of aqueous alteration and evidence for methane generation on the parent bodies of the CM chondrites. Geochim Cosmochim Acta 71(22):5565–5575. https://doi.org/10.1016/j.gca.2007.07.029

Harries D, Langenhorst F (2013) The nanoscale mineralogy of Fe, Ni sulfides in pristine and metamorphosed CM and CM/CI-like chondrites: tapping a petrogenetic record. Meteorit Planet Sci 48(5):879–903. https://doi.org/10.1111/maps.12089

Harries D, Zolensky ME (2016) Mineralogy of iron sulfides in CM1 and CI1 lithologies of the Kaidun breccia: records of extreme to intense hydrothermal alteration. Meteorit Planet Sci 51(6):1096–1109. https://doi.org/10.1111/maps.12648

Hezel DC, Wilden JS, Becker D, Steinbach S, Wombacher F, Harak M (2018) Fe isotope composition of bulk chondrules from Murchison (CM2): constraints for parent body alteration, nebula processes and chondrule-matrix complementarity. Earth Planet Sci Lett 490:31–39. https://doi.org/10.1016/j.epsl.2018.03.013

Hin RC, Schmidt MW, Bourdon B (2012) Experimental evidence for the absence of iron isotope fractionation between metal and silicate liquids at 1 GPa and 1250–1300 ℃ and its cosmochemical consequences. Geochim Cosmochim Acta 93:164–181. https://doi.org/10.1016/j.gca.2012.06.011

Holt MC, Herd CDK (2022) Fe-Ni sulfides in Tagish Lake: implications for nebular and parent body conditions of formation. Meteorit Planet Sci 57(6):1267–1287. https://doi.org/10.1111/maps.13819

Howard KT, Alexander CMO, Schrader DL, Dyl KA (2015) Classification of hydrous meteorites (CR, CM and C2 ungrouped) by phyllosilicate fraction: PSD-XRD modal mineralogy and planetesimal environments. Geochim Cosmochim Acta 149:206–222. https://doi.org/10.1016/j.gca.2014.10.025

Hu ZC, Zhang W, Liu YS, Gao S, Li M, Zong KQ, Chen HH, Hu SH (2015) "Wave" signal-smoothing and mercury-removing device for laser ablation quadrupole and multiple collector ICPMS analysis: Application to lead isotope analysis. Anal Chem 87(2):1152–1157. https://doi.org/10.1021/ac503749k

Kelly DP, Vaughan DJ (1983) Pyrrhotine-pentlandite ore textures: a mechanistic approach. Mineral Mag 47(345):453–463. https://doi.org/10.1180/minmag.1983.047.345.06

Kerraouch I, Bischoff A, Zolensky ME, Pack A, Patzek M, Hanna RD, Fries MD, Harries D, Kebukawa Y, Le L, Ito M, Rahman Z (2021) The polymict carbonaceous breccia Aguas Zarcas: a potential analog to samples being returned by the OSIRIS-REx and Hayabusa2 missions. Meteorit Planet Sci 56(2):277–310. https://doi.org/10.1111/maps.13620

Kerraouch I, Kebukawa Y, Bischoff A, Zolensky ME, Wölfer E, Hellmann JL, Ito M, King A, Trieloff M, Barrat JA, Schmitt-Kopplin P, Pack A, Patzek M, Hanna RD, Fockenberg T, Marrocchi Y, Fries M, Mathurin J, Dartois E, Duprat J, Kondo M (2022) Heterogeneous nature of the carbonaceous chondrite breccia Aguas Zarcas-cosmochemical characterization and origin of new carbonaceous chondrite lithologies. Geochim Cosmochim Acta 334:155–186. https://doi.org/10.1016/j.gca.2022.07.010

Kitakaze A, Sugaki A, Itoh H, Komatsu R (2011) A revision of phase relations in the system Fe-Ni-s from 650 to 450 c. Can Mineral 49(6):1687–1710. https://doi.org/10.3749/canmin.49.6.1687

Lauretta DS, Fegley BJ, Lodders K (1996) The kinetics and mechanism of iron sulfide formation in the solar nebula. Antarct Meteorite Res 9:111

Lauretta DS, Hergenrother CW, Chesley SR, Leonard JM, Pelgrift JY, Adam CD, Al Asad M, Antreasian PG, Ballouz RL, Becker KJ, Bennett CA, Bos BJ, Bottke WF, Brozović M, Campins H, Connolly HC Jr, Daly MG, Davis AB, de León J, DellaGiustina DN, Drouet d'Aubigny CY, Dworkin JP, Emery JP, Farnocchia D, Glavin DP, Golish DR, Hartzell CM, Jacobson RA, Jawin ER, Jenniskens P, Kidd JN Jr, Lessac-Chenen EJ, Li JY, Libourel G, Licandro J, Liounis AJ, Maleszewski CK, Manzoni C, May B, McCarthy LK, McMahon JW, Michel P, Molaro JL, Moreau MC, Nelson DS, Owen WM Jr, Rizk B, Roper HL, Rozitis B, Sahr EM, Scheeres DJ, Seabrook JA, Selznick SH, Takahashi Y, Thuillet F, Tricarico P, Vokrouhlický D, Wolner CWV (2019) Episodes of particle ejection from the surface of the active asteroid (101955) Bennu. Science 366(6470):eaay3544. https://doi.org/10.1126/science.aay3544

Lee MR, Ellen R (2008) Aragonite in the Murray (CM2) carbonaceous chondrite: implications for parent body compaction and aqueous alteration. Meteorit Planet Sci 43(7):1219–1231. https://doi.org/10.1111/j.1945-5100.2008.tb01124.x

Lentfort S, Bischoff A, Ebert S, Patzek M (2021) Classification of CM chondrite breccias: implications for the evaluation of samples from the OSIRIS-REx and Hayabusa 2 missions. Meteorit Planet Sci 56(1):127–147. https://doi.org/10.1111/maps.13486

Liu J, Dauphas N, Roskosz M, Hu MY, Yang H, Bi WL, Zhao JY, Alp EE, Hu JY, Lin JF (2017) Iron isotopic fractionation between silicate mantle and metallic core at high pressure. Nat Commun 8:14377. https://doi.org/10.1038/ncomms14377

Liu SQ, Li YB, Li MH, Yang ZM, Liu JM, Shen YN (2022) Equilibrium fractionation of S, Fe, and Ni isotopes in Fe-Ni sulfides: a first-principles investigation. Chem Geol 610:121100. https://doi.org/10.1016/j.chemgeo.2022.121100

Lü XT, He DT, Liu YS, Li M, Lin J, Chen W, Zhu L, Yang A, Feng YT, Liu ZY, Zeng XL, Hu ZC (2024) *In situ* Fe isotope analysis of Cr-rich iron oxides using pure chromium metal for isobaric interference corrections by femtosecond LA–MC–ICP–MS. Chem Geol 648:121935. https://doi.org/10.1016/j.chemgeo.2024.121935

Meftah N, Mostefaoui S, Jambon A, Guedda EH, Pont S (2016) Minor and trace element concentrations in adjacent kamacite and taenite in the Krymka chondrite. Meteorit Planet Sci 51(4):696–717. https://doi.org/10.1111/maps.12617

Nakanishi N, Yokoyama T, Okabayashi S, Iwamori H, Hirata T (2022) Geochemical constraints on the formation of chondrules: implication from Os and Fe isotopes and HSE abundances in metals from CR chondrites. Geochim Cosmochim Acta 319:254–270. https://doi.org/10.1016/j.gca.2021.11.009

Naldrett A (1989) Magmatic sulfide deposits. In: Oxford monographs on geology and geophysics, No 14. Oxford University Press. New York, pp 186

Ni P, Chabot NL, Ryan CJ, Shahar A (2020) Heavy iron isotope composition of iron meteorites explained by core crystallization. Nat Geosci 13(9):611–615. https://doi.org/10.1038/s41561-020-0617-y

Okabayashi S, Yokoyama T, Nakanishi N, Iwamori H (2019) Fractionation of highly siderophile elements in metal grains from unequilibrated ordinary chondrites: implications for the origin of chondritic metals. Geochim Cosmochim Acta 244:197–215. https://doi.org/10.1016/j.gca.2018.10.003

Polyakov VB (2009) Equilibrium iron isotope fractionation at core-mantle boundary conditions. Science 323(5916):912–914. https://doi.org/10.1126/science.1166329

Polyakov VB, Soultanov DM (2011) New data on equilibrium iron isotope fractionation among sulfides: constraints on mechanisms of sulfide formation in hydrothermal and igneous systems. Geochim

Cosmochim Acta 75(7):1957–1974. https://doi.org/10.1016/j.gca.2011.01.019
Polyakov VB, Clayton RN, Horita J, Mineev SD (2007) Equilibrium iron isotope fractionation factors of minerals: reevaluation from the data of nuclear inelastic resonant X-ray scattering and Mössbauer spectroscopy. Geochim Cosmochim Acta 71(15):3833–3846. https://doi.org/10.1016/j.gca.2007.05.019
Polyakov VB, Osadchii EG, Voronin MV, Osadchii VO, Sipavina LV, Chareev DA, Tyurin AV, Gurevich VM, Gavrichev KS (2019) Iron and sulfur isotope factors of pyrite: data from experimental mössbauer spectroscopy and heat capacity. Geochem Int 57(4):369–383. https://doi.org/10.1134/s0016702919040098
Raghavan V (2004) Fe-Ni-S (Iron-Nickel-Sulfur). J Phase Equilib Diffus 25:373–381
Rubin AE, Trigo-Rodríguez JM, Huber H, Wasson JT (2007) Progressive aqueous alteration of CM carbonaceous chondrites. Geochim Cosmochim Acta 71(9):2361–2382. https://doi.org/10.1016/j.gca.2007.02.008
Saunier G, Pokrovski GS, Poitrasson F (2011) First experimental determination of iron isotope fractionation between hematite and aqueous solution at hydrothermal conditions. Geochim Cosmochim Acta 75(21):6629–6654. https://doi.org/10.1016/j.gca.2011.08.028
Schauble EA (2004) Applying stable isotope fractionation theory to new systems. Rev Mineral Geochem 55(1):65–111. https://doi.org/10.2138/gsrmg.55.1.65
Schiller M, Bizzarro M, Siebert J (2020) Iron isotope evidence for very rapid accretion and differentiation of the proto-Earth. Sci Adv 6(7):eaay7604. https://doi.org/10.1126/sciadv.aay7604
Schuessler JA, Schoenberg R, Behrens H, von Blanckenburg F (2007) The experimental calibration of the iron isotope fractionation factor between pyrrhotite and peralkaline rhyolitic melt. Geochim Cosmochim Acta 71(2):417–433. https://doi.org/10.1016/j.gca.2006.09.012
Schrader DL, Connolly HC Jr., Lauretta DS, Zega TJ, Davidson J, Domanik KJ (2015) The formation and alteration of the Renazzo-like carbonaceous chondrites III: toward understanding the genesis of ferromagnesian chondrules. Meteorit Planet Sci 50(1):15–50. https://doi.org/10.1111/maps.12402
Schrader DL, Davidson J, McCoy TJ (2016) Widespread evidence for high-temperature formation of pentlandite in chondrites. Geochim Cosmochim Acta 189:359–376. https://doi.org/10.1016/j.gca.2016.06.012
Schrader DL, Fu RR, Desch SJ, Davidson J (2018) The background temperature of the protoplanetary disk within the first four million years of the Solar System. Earth Planet Sci Lett 504:30–37. https://doi.org/10.1016/j.epsl.2018.09.030
Schrader DL, Zega TJ (2019) Petrographic and compositional indicators of formation and alteration conditions from LL chondrite sulfides. Geochim Cosmochim Acta 264:165–179. https://doi.org/10.1016/j.gca.2019.08.015
Schrader DL, Davidson J, McCoy TJ, Zega TJ, Russell SS, Domanik KJ, King AJ (2021) The Fe/S ratio of pyrrhotite group sulfides in chondrites: an indicator of oxidation and implications for return samples from asteroids Ryugu and Bennu. Geochim Cosmochim Acta 303:66–91. https://doi.org/10.1016/j.gca.2021.03.019
Scott SR, Sims KWW, Frost BR, Kelemen PB, Evans KA, Swapp SM (2017) On the hydration of olivine in ultramafic rocks: implications from Fe isotopes in serpentinites. Geochim Cosmochim Acta 215:105–121. https://doi.org/10.1016/j.gca.2017.07.011
Singerling SA, Brearley AJ (2018) Primary iron sulfides in CM and CR carbonaceous chondrites: insights into nebular processes. Meteorit Planet Sci 53(10):2078–2106. https://doi.org/10.1111/maps.13108
Singerling SA, Brearley AJ (2020) Altered primary iron sulfides in CM2 and CR2 carbonaceous chondrites: insights into parent body processes. Meteorit Planet Sci 55(3):496–523. https://doi.org/10.1111/maps.13450
Sossi PA, Nebel O, Foden J (2016) Iron isotope systematics in planetary reservoirs. Earth Planet Sci Lett 452:295–308. https://doi.org/10.1016/j.epsl.2016.07.032
Velbel MA, Palmer EE (2011) Fine-grained serpentine in CM2 carbonaceous chondrites and its implications for the extent of aqueous alteration on the parent body: a review. Clays Clay Miner 59(4):416–432. https://doi.org/10.1346/ccmn.2011.0590405
Visser R, John T, Patzek M, Bischoff A, Whitehouse MJ (2019) Sulfur isotope study of sulfides in CI, CM, $C2_{ung}$ chondrites and volatile-rich clasts–evidence for different generations and reservoirs of sulfide formation. Geochim Cosmochim Acta 261:210–223. https://doi.org/10.1016/j.gca.2019.06.046
Wang K, Moynier F, Barrat JA, Zanda B, Paniello RC, Savage PS (2013) Homogeneous distribution of Fe isotopes in the early solar nebula. Meteorit Planet Sci 48(3):354–364. https://doi.org/10.1111/maps.12060
Weyer S, Anbar AD, Brey GP, Münker C, Mezger K, Woodland AB (2005) Iron isotope fractionation during planetary differentiation. Earth Planet Sci Lett 240(2):251–264. https://doi.org/10.1016/j.epsl.2005.09.023
Yang X, Hanna RD, Davis AM, Neander AI, Heck PR (2022) A record of post-accretion asteroid surface mixing preserved in the Aguas Zarcas meteorite. Nat Astron 6(9):1051–1058. https://doi.org/10.1038/s41550-022-01746-4
Zanda B, Bourot-Denise M, Hewins RH (1995) Condensate sulfide and its metamorphic transformations in primitive chondrites. Meteoritics 30(5):605
Zeng ZG, Li XH, Chen S, de Jong J, Mattielli N, Qi HY, Pearce C, Murton BJ (2021) Iron, copper, and zinc isotopic fractionation in seafloor basalts and hydrothermal sulfides. Mar Geol 436:106491. https://doi.org/10.1016/j.margeo.2021.106491
Zhu XK, Guo Y, O'Nions RK, Young ED, Ash RD (2001) Isotopic homogeneity of iron in the early solar nebula. Nature 412(6844):311–313. https://doi.org/10.1038/35085525
Zhu K, Moynier F, Alexander CMO (2021) Chromium isotopic evidence for evaporation during enstatite chondrite formation. Astrophys J 923:94. https://doi.org/10.3847/1538-4357/ac2570
Zolensky ME, Mittlefehldt DW, Lipschutz ME, Wang MS, Clayton RN, Mayeda TK, Grady MM, Pillinger C, David B (1997) CM chondrites exhibit the complete petrologic range from type 2 to 1. Geochim Cosmochim Acta 61(23):5099–5115. https://doi.org/10.1016/S0016-7037(97)00357-8